Nanoscale domain evolution in thin films of multiferroic $TbMnO_3$

Sriram Venkatesan, Christophe Daumont, Bart J. Kooi,* Beatriz Noheda, and Jeff. Th. M. De Hosson
Zernike Institute for Advanced Materials, University of Groningen, Nijenborgh 4, 9747 AG Groningen, The Netherlands
(Received 1 September 2009; revised manuscript received 2 November 2009; published 14 December 2009)

Control of the domain structures in multiferroic thin films is of crucial importance in order to gain access to their functional responses. Here we report on the evolution of the nanodomain structures observed in epitaxial thin films of multiferroic $TbMnO_3$ grown on $SrTiO_3$ substrates. Thin films with thickness ranging from 2 to 140 nm were grown at 0.25 and 0.9 mbar oxygen partial pressures. Transmission electron microscopy was employed to study and understand the domain evolution. A transition from a fully coherent, highly strained, tetragonal film to a partially coherent, distorted, orthorhombic structure occurs via a transformation twinning mechanism, giving rise to four different domain orientations. Then, at larger thicknesses, a transition to the fully relaxed orthorhombic structure occurs via changes in the domain-substrate orientation relationships leading to only two domain variants. Differences have been observed in the strain relaxation behavior for films grown at different oxygen pressures. All the observations have allowed us to understand the evolution of the domain structures and to accurately explain the measured orthorhombic distortion. This mechanism can be generalized for [001]-oriented orthorhombic perovskites grown on cubic substrates with large misfit values.

DOI: 10.1103/PhysRevB.80.214111 PACS number(s): 68.55.−a, 68.37.Lp, 61.72.Mm, 68.60.Bs

I. INTRODUCTION

Perovskite manganites with a strong coupling between spontaneous electrical and magnetic polarizations are a topic of severe current interest because of their fundamental scientific importance and prospective technological applications in magnetoelectric (ME) devices.[1,2] Bulk multiferroics of rare-earth substituted manganites, $RMnO_3$ (R=rare-earth element), display two-crystal structures depending on the size of the R ion: orthorhombic for R=La-Dy and hexagonal for Ho-Lu. The orthorhombic $TbMnO_3$ (TMO) is receiving much attention because of its coupling between the magnetic spin structure and electrical degrees of freedom resulting in a strong ME effect.[3] At room temperature, bulk TMO has a perovskite crystal structure (space group Pbnm) with lattice parameters a=5.2931 Å, b=5.8384 Å, and c=7.4025 Å.[4] Below $T_N \approx 42$ K, $TbMnO_3$ shows a sinusoidal antiferromagnetic order, which appears from a subtle balance between ferromagnetic (FM) and antiferromagnetic (AFM) exchange constants between different Mn neighbors. Additionally, below $T_{FE} \approx 28$ K the spin arrangement changes into a spiral structure, which breaks inversion symmetry, and ferroelectricity comes into play with a polarization parallel to the c axis. Thus, even though TMO does not exhibit net magnetization, it has been considered an interesting candidate for multiferroic devices based on exchange bias.[3,5,6]

However, recently, an interesting development has taken place: $TbMnO_3$ and other manganites in thin film form exhibit a net magnetic moment when strained on a cubic substrate.[7–9] Different origins have been proposed for the net magnetization; two of these are the most prominent ones: (1) epitaxial strain changes the balance between AFM and FM interactions, inducing a net magnetization[8] and (2) ferromagnetism originates at the domain walls, which gives rise to a different structure than that of the domains themselves and are present in large quantities in the thin films.[10] To discriminate between these two mechanisms is not easy because of the difficulty to image magnetism at such small length scales and because of the direct relationship between the density of domain walls and the epitaxial strain.[11] These developments indicate that, for a proper understanding of the properties of the thin films, knowledge of the domain structures is a prerequisite.

Depending on the difference between the substrate's and film's lattice parameters, tensile and/or compressive strains can be imposed onto the film. This situation holds true only up to a specific critical thickness, which varies per system depending on the misfit strain accommodation mechanisms and of the substrate-film combination.[12] A further increase in the film thickness will result in loss of coherency strains of the film and relaxation starts, for instance, by formation of misfit (and/or threading) dislocations or by breaking into different (mutually relaxing) domains. Domain boundaries break inversion symmetry and thus, in ferroic systems, they show different properties than the domains themselves. Accumulation of defects, or the particular local structure of the walls, can also give rise to different transport properties.[13] Therefore, the control of the domain structures in thin films is of crucial importance to increase and tune the functionality of ferroic thin films. In the present work we investigate the nanoscale evolution of domain structures present in TMO films grown on $SrTiO_3$ (STO) substrates with increasing thickness and we show that it is possible to rationalize the observed structures and their evolution as a direct result of the epitaxial strain.

Perovskite TMO thin films with orthorhombic structure have been investigated scarcely until now. Figures 1(a) and 1(b) show the atomic model of the unit cell of bulk orthorhombic $TbMnO_3$ and its projection along the c axis, respectively. Figure 1(c) shows the atomic model of the (001) plane of cubic $SrTiO_3$; this is the surface on which the $TbMnO_3$ thin films grow. Detailed x-ray diffraction (XRD) and magnetization measurements have been reported elsewhere.[7,9,10] The structural investigation by XRD provides macroscopic volume-averaged information. On the contrary, transmission electron microscopy (TEM) has the advantage of high spatial

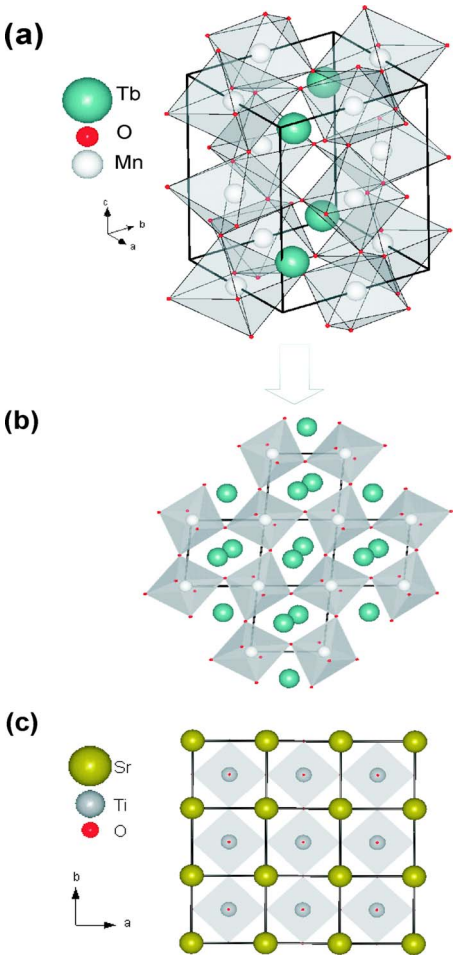

FIG. 1. (Color online) Atomic-structure model showing (a) unit cell of (bulk) orthorhombic $TbMnO_3$, (b) projection of the (bulk) orthorhombic $TbMnO_3$ crystal along its *c* axis, and (c) the top view of cubic $SrTiO_3$, representing the surface on which the $TbMnO_3$ thin films grow.

resolution which can provide information on structure, symmetry, domain sizes, domain shapes, and domain-wall orientations on a local scale. Such a report of the detailed domain structure evolution at nanoscale of TMO was lacking and is the present focus of this paper.

II. EXPERIMENT

Phase pure orthorhombic TMO thin films of different thicknesses were grown using pulsed laser deposition (KrF excimer laser $\lambda = 248$ nm) assisted by reflection high-energy electron diffraction (RHEED) from stoichiometric targets. Epitaxial growth occurred on properly treated (001)-oriented STO substrates with atomically flat terraces of one unit-cell step height. The films were grown at 750 °C and at 1 Hz laser pulse frequency with laser fluence of 2 J/cm^2. The films were cooled to room temperature at −3 °C per minute under a 100 mbar of O_2. One set of films with various thicknesses (17, 34, 67, and 140 nm) were grown at 0.25 mbar oxygen partial pressure and another set of films (15, 30, and 60 nm) were grown at 0.9 mbar oxygen partial pressure, keeping the other growth parameters constant.[10]

The plane-view and cross-sectional TEM observations of the thin films were performed using a JEOL 2010F electron microscope operating at 200 kV. The specimen preparation for TEM observation involves a conventional procedure of cutting, grinding, polishing, dimpling, and ion milling. The samples were thinned down to electron transparency using a precision ion polishing system (Gatan model 491) with two ion guns of 4 kV Ar^+ beams at an angle of 8°. For plane-view specimens both ion guns are focused at the bottom side of the substrate. The other side of the film is covered with a piece of glass to avoid any contamination by redeposition from the sputtered backside. For cross-section specimens both sides were ion milled.

III. RESULTS AND DISCUSSION

A. Nanodomain structures in thin TMO films

Microstructure analysis of the thin films grown at different thickness can explain the strain accommodation of orthorhombic TMO on cubic STO, including the evolution of the domain structures and the film-substrate orientation relationships. When compared to the length of the STO[110] vector, the orthorhombic lattice parameter *b* is under compressive strain with a lattice mismatch of about 5.7% and the lattice parameter *a* is under tensile strain with a mismatch of about 4.1%. From the TEM images and XRD patterns,[10] we infer that TMO always grows with its *c* axis perpendicular to the STO (001) surface and, therefore, the projections shown in Figs. 1(b) and 1(c) are relevant.

TEM analysis of plane-view bright-field images and selected-area electron diffraction patterns as depicted in Figs. 2(a) and 3(a) show that the 17 nm TMO film is epitaxially strained and partially coherent with the STO substrate. The TMO has a (distorted) orthorhombic structure. The film consists of rectangular nanodomains with a relatively large aspect ratio (5:1), forming two sets of perpendicular twins. A combination of images and diffraction patterns indicates that the domain walls parallel to the long (in-plane) axis of the domains, correspond to TMO (110) or $(1\bar{1}0)$ planes. The orientation relation with the substrate is such that these TMO planes are parallel to the STO (100) and (010). Since the TMO (110) and $(1\bar{1}0)$ planes are not orthogonal (their mutual angle is 84.4° in the bulk structure, whereas for STO (100) and (010) it is of course 90°), four domain variants develop in the form of the two sets of twins.[10] The superposition of four diffuse diffraction spots, centered around the substrate diffraction spots, forms a cross pattern in the electron diffraction pattern and confirms the presence of four domain variants.

The diffuse (not sharp) contrast of the domain walls in the plane-view TEM image is caused by the influence of the strain fields, largely associated with the coherency strains, on the TEM diffraction contrast. From plane-view images it is measured that the average domain area of this 17-nm-thick film corresponds to 105 ± 10 nm^2. The cross-section high-resolution TEM image of the film shows a sharp substrate-film interface which is free from (an array of) misfit disloca-

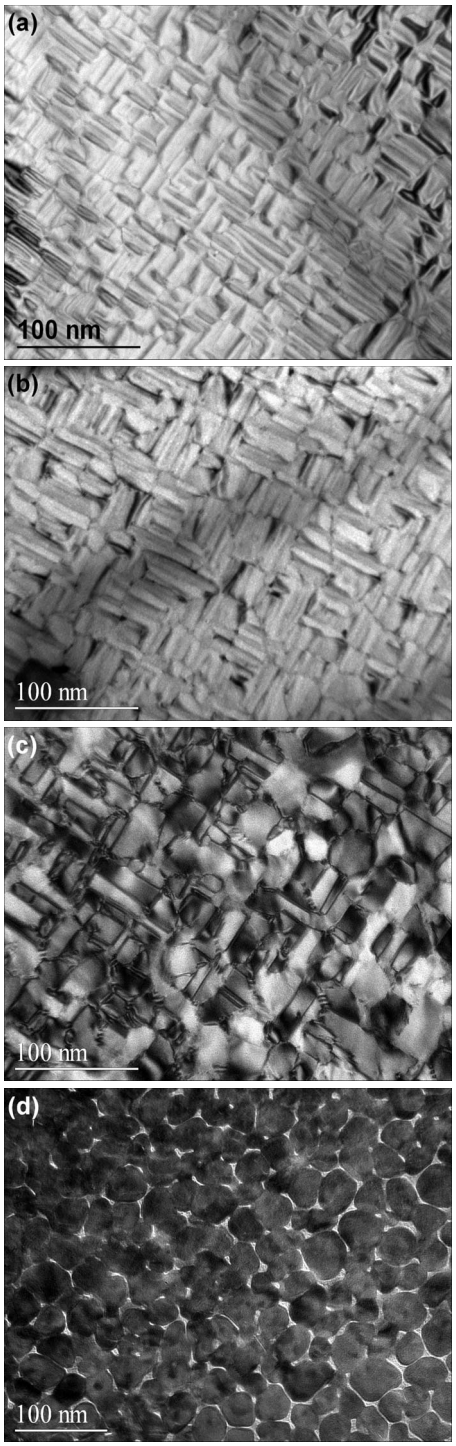

FIG. 2. Bright-field plane-view TEM micrographs of $TbMnO_3$ thin films on $SrTiO_3$ substrates grown at 0.25 mbar oxygen partial pressure with thickness (a) 17, (b) 34, (c) 67, and (d) 140 nm. Micrographs show the evolution of domain structures with increasing film thicknesses.

tions. This confirms the epitaxial and coherent growth of the film, where coherency strain field contrast is, for instance, visible at the right side of the interface in Fig. 4(a).

Compared to the 17 nm film, the domains in the 34 nm film have grown to an average area of about 205 ± 15 nm^2, have become less elongated (reduced aspect ratio) and also

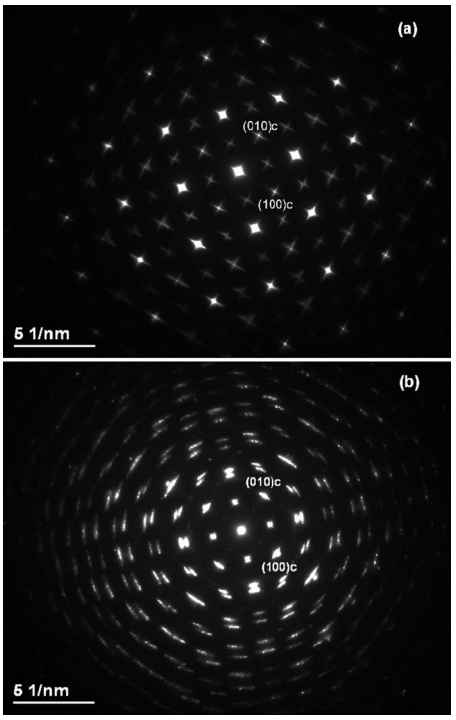

FIG. 3. Selected area electron diffraction pattern of $TbMnO_3$ thin films on $SrTiO_3$ substrates with thickness of (a) 17 nm, showing cross patterns confirming the presence of the four domain variants determined by x-ray diffraction; (b) 67 nm, showing arcs that confirm the in-plane rotations present between domains.

the coherency strains as deduced from the TEM diffraction contrast images are slightly reduced. The enhanced sharpness of the domain walls in the image shown in Fig. 2(b) is due to the reduced strain fields. This indicates that the elastic strain in the film is lower than the strain present in the 17 nm film. The presence of four domain variants is still valid, even for the doubled thickness.

1. Transition from tetragonal to distorted orthorhombic structure

In case of ultrathin TMO films with a thickness of 2 nm, XRD reveals that the TMO structure is tetragonal with the *c* axis perpendicular to the film surface and in-plane orientations and distances fully coherent with the STO substrate.[10] This can be regarded as orthorhombic TMO with a tensile strain of 4.1% along the *a* axis (parallel to [110]STO) and a compressive strain of 5.7% along the *b* axis (parallel to $[1\bar{1}0]$STO). As explained in the previous section, for thicker films an (partially strained and distorted) orthorhombic structure is observed, where the film breaks up in nanodomains. Intuitively one would expect that a checkerboard domain pattern would develop with domain walls parallel to the TMO(100) and (010) and where alternating the short *a* and the long *b* axes (perpendicular to the walls) would compensate each other; see Fig. 5(a), where the vectors indicate the orientation of the (in-plane) *a* axis of orthorhombic TMO. However, this situation is not observed. Instead, the domain walls are parallel to TMO(110) and $(1\bar{1}0)$ with one clearly longer than the other, resulting in rectangular nanodomains

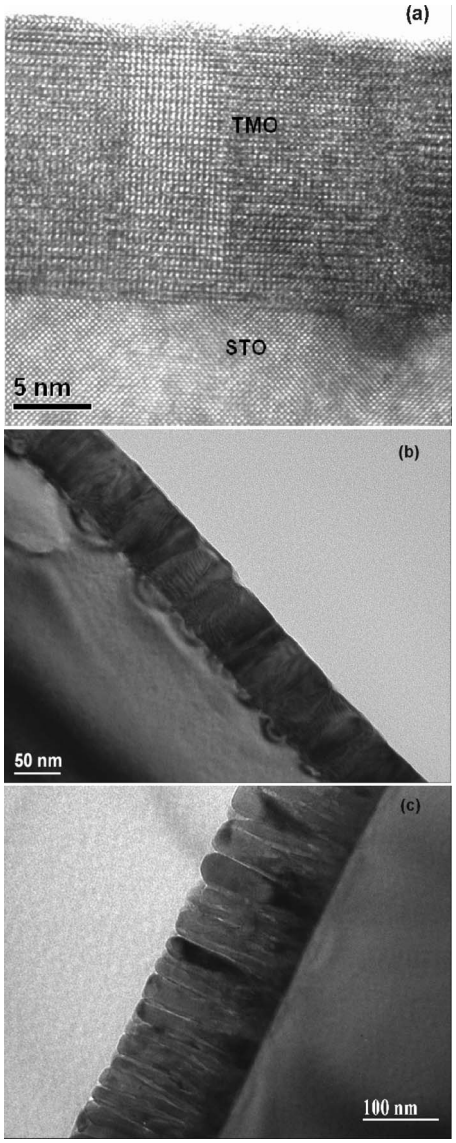

FIG. 4. Bright-field cross-section TEM micrographs of $TbMnO_3$ thin films on $SrTiO_3$ substrates grown at 0.25 mbar oxygen partial pressure with thickness (a) 17 nm, showing a high resolution image of the substrate-film interface with a strain field contrast on the right hand side of the interface; (b) 67 nm, showing columnar growth along with long range strain fields at the substrate film interface; and (c) 140 nm, showing open columnar structure with relatively deep cusps at the column boundaries.

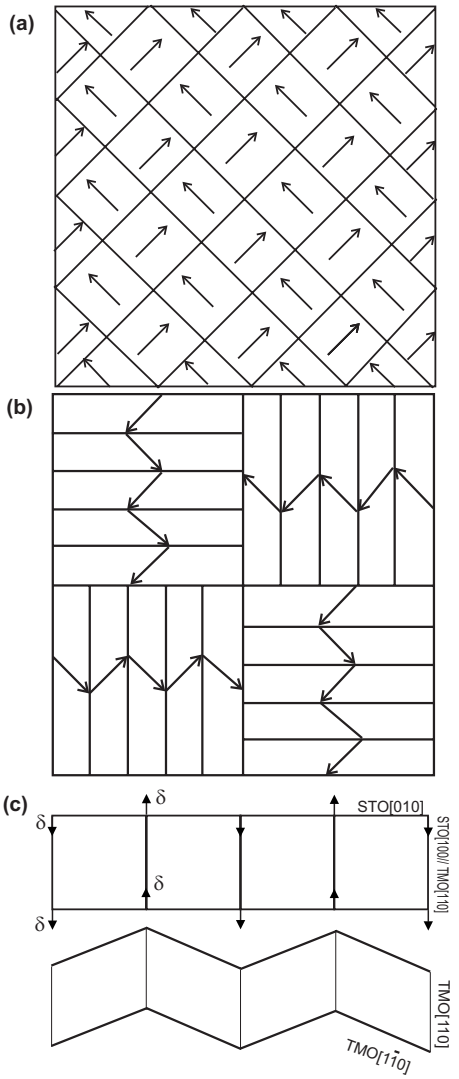

FIG. 5. Schematic for domain structure in $TbMnO_3$ film showing (a) (not observed) checker board pattern indicating the orientation of the *a* (or *b*) vector in the various domains separated by (100) and (010) domain walls, (b) (observed) twin structure with four sets of zigzag patterns; the orientation of the *a* vectors in the various domains separated by (110) and (1$\bar{1}$0) domain walls is indicated (c) explanation of the twinning process, where the shear vector δ operates on the initially tetragonal TMO fully coherent with the STO substrate (shown on the top) in order to form the distorted orthorhombic TMO partially coherent with the STO (shown at the bottom).

with relatively large aspect ratio, as described above.

Initially, for film thicknesses around 15 nm, coherency is fully maintained parallel to the long (in-plane) [110] or [1$\bar{1}$0] axes of the rectangular domains; [110]TMO=[200]STO or [1$\bar{1}$0]TMO=[020]STO. With respect to bulk TMO, a compressive strain of 0.9% is required to maintain this coherency, i.e., already much lower than the ~5% required to maintain the tetragonal structure. If the [110] axis is the fully coherent direction, then the [1$\bar{1}$0], which deviates about 6° from the perpendicular direction, stays over longer distances in registry with the cubic substrate by alternating short segments with plus and minus 6° deviations; see Fig. 5(b). So, if full coherence is maintained along the [110]TMO =[200]STO, the [1$\bar{1}$0] is slightly longer (less compressively strained) since adding up one plus and one minus 6° [1$\bar{1}$0] vector of the zigzag corresponds to [040]STO. Effectively, this means that there is a coherency strain of about 0.4% in this [040] direction.

The principal reasons why the checkerboard pattern in Fig. 5(a) is not observed, but the pattern in Fig. 5(b) is observed are the following: (i) the domains in Fig. 5(a) cannot be associated with a partial coherence with the substrate, whereas the domains in Fig. 5(b) can and (ii) the domains in

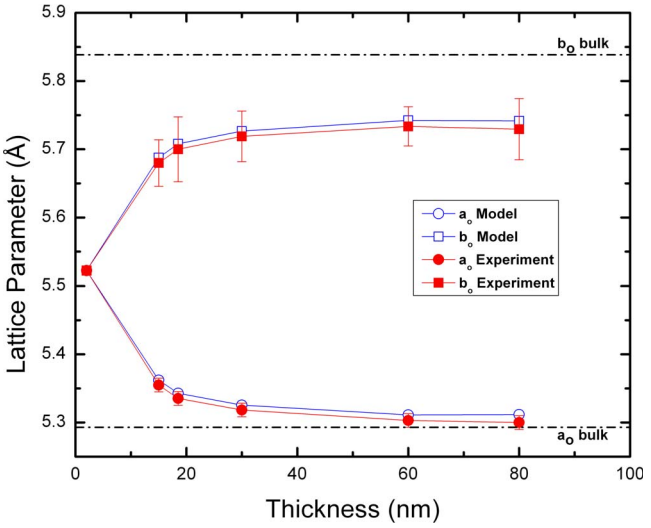

FIG. 6. (Color online) Graph showing an excellent agreement between experimentally determined and predicted (Ref. 14) lattice parameters of orthorhombic $TbMnO_3$ thin films plotted as a function of film thickness.

Fig. 5(a) cannot be associated with a tiling that fulfills the compatibility requirement, where the original surface area is fully covered by the domains without the formation of gaps (or overlaps) between them, whereas the domains in Fig. 5(b) can.

The transition in the TMO film from the tetragonal to the orthorhombic structure and the breaking up in domains clearly indicates a twinning operation. The shear displacements associated with the twinning process are schematically indicated in Fig. 5(c). This shearing process and the coherency conditions followed during this twinning operation results in a distortion of the orthorhombic TMO such that the principal lattice vectors a and b do not become orthogonal. Taking $a_{STO}\sqrt{2}$ as starting condition, the decrease in the a lattice parameter of TMO and the increase in the b lattice parameter are nearly identical, such that the b lattice parameter will always deviate stronger from its bulk value than the a lattice parameter (see Fig. 6).

The observed nanodomain structures strongly suggest a twinning mechanism, but proof for this mechanism comes from the excellent quantitative agreement between predicted and measured XRD data[10] (see Fig. 6). The only unknown parameter in the twinning process is the relative length of the shear vector δ (cf. Fig. 5(c)). This single parameter fully determines the distorted orthorhombic structure, i.e., the deviations from the bulk values.[14] Based on the value for the pseudocubic angle γ,[7] we derive the value for δ and then we calculate, without any adjustable parameter, the lattice parameters a and b,[14] leading for the various film thicknesses to the excellent agreement shown in Fig. 6. This analysis shows that the shear vector δ increases with film thickness such that the pseudocubic angle γ and the lattice parameters a and b approach bulk values and thus indicates a reduced distortion and therefore a structural relaxation behavior.

However, simultaneously, the angle between the a and b vectors shows an increasing deviation from 90° and thus leads to an increasing, although relatively small structural distortion; too small to be observed in our XRD experiments.[10] The angle between a and b can be calculated from $\text{atan}(1+2\delta/3.905)+\text{atan}(1-2\delta/3.905)$ with the δ in Å. More importantly, this mechanism does not allow a full relaxation of the b lattice parameter (cf. Fig. 6). A further increase in δ would relax the b lattice parameter, but then the a lattice parameter and the pseudocubic angle γ would decrease below their bulk values. Therefore, this mechanism of an increasing shear vector is running into a dead alley and a second structural transformation, explained in the next section, is required that can really lead to a completely relaxed orthorhombic structure.

2. Disappearance of the distortion in the orthorhombic structure

Remarkable changes occur with respect to the domain shape and size when the film thickness is increased from 34 to 67 nm; compare Figs. 2(b) and 2(c). In addition to the rectangular domains, now also nearly circular (coalesced) domains can be seen in the plane-view TEM image [Fig. 2(c)]. The domain area reaches about 320 ± 20 nm^2 on average and domains have a much reduced aspect ratio. The sharp contrast of the domain walls in the image is due to the smaller magnitude of strain fields, where the top of the film for the circular coalesced grains become relaxed.

The 67-nm-thick film shows an intermediate stage where the coalesced grains adopt a new orientation relationship (OR) not present in the thinner films. Due to the reduced elastic strain, the domains tend toward an energetically more stable configuration with two domain variants, i.e., (100) and (010) of the orthorhombic film parallel to the (110) and $(1\bar{1}0)$ of the cubic substrate, instead of four variants. Evidence of this has been also obtained by XRD.[10] In principle, the change in OR is only related to a slight in-plane rotation of about 3°. The development of this new OR allows the removal of the distortion of the orthorhombic structure such that (i) the b vector can relax to its bulk value and (ii) the a and b vectors can become orthogonal and thus allows a complete strain relaxation to the bulk orthorhombic unit cell not possible by the twinning process delineated in the previous section.

The electron diffraction pattern of the 67-nm-thick film, depicted in Fig. 3(b), shows that the TMO domains/grains exhibit relatively large mutual in-plane rotations (i.e., around their common c axis). Cross-section bright-field TEM images of the 67-nm-thick film show columnar grains [see Fig. 4(b)], where the top of the columns are still relatively flat. The height variation in the 67-nm-thick film around the domain/column boundaries observable in Fig. 4(b) are larger than in the 17 nm film [Fig. 4(a)], but develop clearly to cusps in the 140-nm-thick film [Fig. 4(c)]. For the latter thickness the column structure is clearly more developed and the top of the columns approach a dome structure. In the cross-section images shown in Figs. 4(a)–4(c) it is observable that relatively large sized strain fields are still present at the substrate-film interface indicating that the foot of each column is always partially coherent and that arrays of misfit dislocations at the film-substrate interface are absent. Particularly in Fig. 4(b) for the 67-nm-thick film, the long-range strain fields, extending into the STO substrate with a similar

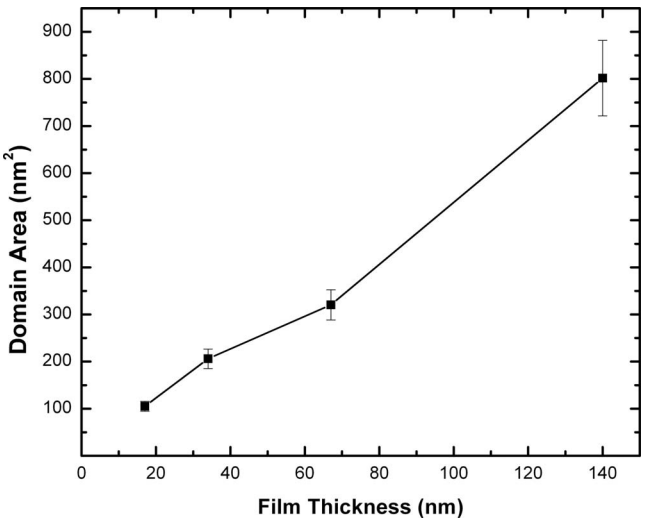

FIG. 7. Plot showing the average surface area of the $TbMnO_3$ domains measured from plane-view TEM images, increases linearly with increasing thickness.

range as the width of the columns, are clearly visible.

The bright-field plane-view and cross-section TEM image of the 140 nm thick film, depicted in Figs. 2(d) and 4(c), show that the growth is completely columnar and that the shape of the domains (now grains) in plane view are nearly circular. Relatively deep cusps are present at the column boundaries, which also appear to have a more open structure. These columns are still strained to maintain the partial coherence at the substrate-film interface. Approximately up to 30 nm, the compressive strain parallel to the film-substrate interface are transferred across the column boundaries. Above ~30 nm the columns start to grow independently and the column boundaries allow strain relaxation. In this first 30 nm also growth selection occurs, where some columns grow broader at the expense of other columns which become thinner and even can disappear. The average grain area of the 140-nm-thick film as measured based on plane-view images is $\sim 800 \pm 40$ nm^2. The evolution of domain size with film thickness is shown in Fig. 7.

Characterization of these domain structures is crucial to understand the functional properties of the films and their characterization using local probe methods may reveal the essential contribution of the domain walls.[15]

B. Role of oxygen partial pressure

The 30 nm film grown in 0.9 mbar oxygen pressure has similar structure as the thinner (17 and 34 nm) films grown in 0.25 mbar. Compared to the films grown in 0.25 mbar, the films grown at 0.9 mbar oxygen pressure relax the strains due to partial coherence at a relatively lower thickness. Figures 8(a) and 8(b) show cross-section TEM images of a 60 nm film grown in 0.9 mbar. The film exhibits a well-developed columnar structure with relatively deep cusps at the column boundaries. This structure does not resemble the one observed for a film of similar thickness grown in 0.25 mbar (compare Figs. 8(a), 8(b), and 4(b)). Instead, the 60 nm 0.9 mbar film has a similar structure as the 140 nm 0.25 mbar film (compare Figs. 8(a), 8(b), and 4(c)). The bright-field TEM image of the 60 nm film grown at 0.9 mbar, shown in Fig. 8(c), exhibits high density moiré patterns. The moiré fringes occur due to the interference of two crystal lattices with small mutual rotation and/or differences in lattice constants. The observation of these fringes, not present in case of the films grown in 0.25 mbar, is direct evidence for the presence of misfit dislocation at the substrate-film interface. This is corroborated by our cross-section TEM images, where instead of a single long-range strain field per column, there are many more also very localized (small) strain fields present that can be associated with arrays of misfit dislocations [see Fig. 8(b)].

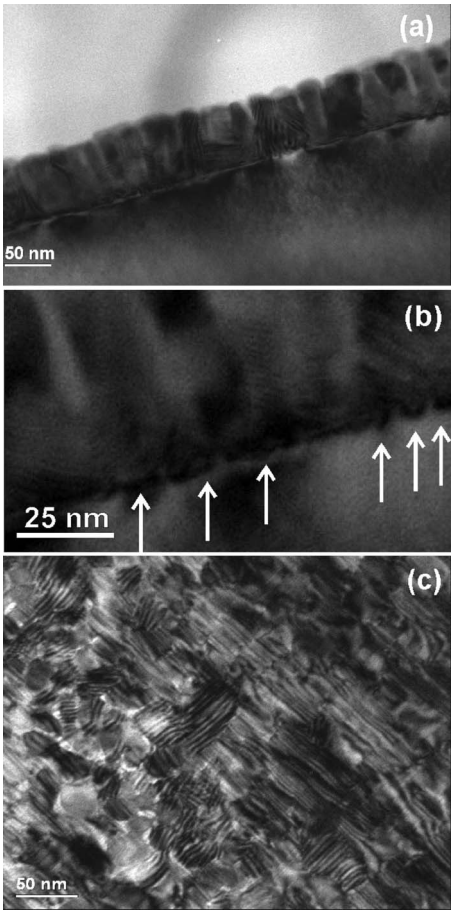

FIG. 8. Bright-field TEM micrographs of $TbMnO_3$ thin films on $SrTiO_3$ substrates grown at 0.9 mbar oxygen partial pressure with a thickness of 60 nm: (a) Overview cross-section image showing columnar growth with localized strain fields; (b) magnified cross-section image showing in more detail the strain field contrast of misfit dislocations (examples indicated by arrows). (c) Plane-view TEM micrograph of a 60 nm $TbMnO_3$ thin film on $SrTiO_3$ substrate grown at 0.9 mbar oxygen partial pressure showing high density moiré patterns resulting from mutual rotations and/or differences in lattice constants of TMO and STO. Note that these moiré patterns were not observed in plane-view TEM micrographs of TMO film on STO substrates grown at 0.25 mbar oxygen partial pressure.

In general, perovskite oxide films can accommodate a high concentration of oxygen vacancies without losing its perovskite structure. The possibility of a significant concentration of oxygen vacancies in the films grown at an oxygen

partial pressure of 0.25 mbar cannot be totally ruled out even though our XPS measurement does not show evidence of Mn^{2+}. Assuming that the oxygen vacancy concentration in the films grown in 0.25 mbar is clearly higher than in the ones grown in 0.9 mbar, it can also be understood that the critical thickness for strain relaxation is higher in the films grown at 0.25 mbar. The reason is that the vacancy concentration can assist in the strain relaxation such that the remaining strain is lower, so that the driving force for introduction of misfit dislocations is reduced. Moreover, in thicker films strain can be relaxed at the column boundaries. Effectively this means that the strain in the 0.25 mbar films is relaxed by the oxygen vacancies and the column boundaries such that misfit dislocations do not come into play. On the other hand, misfit dislocations appeared unavoidable for providing completely relaxed films in the films grown at the higher oxygen partial pressure of 0.9 mbar (maximum pressure we could reach in our PLD chamber allowing RHEED intensity to be monitored).

IV. CONCLUSIONS

(001)-oriented $TbMnO_3$ thin films, grown epitaxially on (001) $SrTiO_3$ substrates with various thicknesses at different oxygen partial pressures, show a remarkable evolution of nanodomain structures. This evolution can be understood on the basis of an initial tetragonal structure, transforming into a distorted orthorhombic structure by a twinning process. This mechanism gives rise to four domain variants (with [110] or $[1\bar{1}0]$ of TMO parallel to [100] or [010] of STO) above a first critical thickness of about 5 nm, transforming finally into a relaxed (undistorted) orthorhombic structure, which gives rise to two domain variants (with [100] and [010] of TMO parallel to [110] and $[1\bar{1}0]$ of STO) above a second critical thickness of about 60 nm. Knowledge of the twinning mechanism allows accurate prediction and understanding of the measured distortion of the orthorhombic structure and it shows that the symmetry of the strained films is lower than orthorhombic, since a and b are not exactly orthogonal.

TMO films grown at a higher oxygen partial pressure (0.9 mbar) show strain relaxation at lower thickness (60 nm) than films grown at lower pressure (0.25 mbar). This difference is attributed to a higher concentration of oxygen vacancies at lower oxygen partial pressure and therefore a reduced strain. Strain relaxation in the film occurs by two mechanisms: 1) Misfit dislocation formation at the substrate-film interface and 2) the formation of columnar structures with increasing relaxation at the column boundaries with increasing thickness. At 0.9 mbar the first mechanism dominates, whereas at 0.25 mbar the second one occurs.

ACKNOWLEDGMENTS

This work has been funded by the Zernike Institute for Advanced Materials, University of Groningen, The Netherlands. C.J.M.D. and B.N. gratefully acknowledge the EU STREP project MaCoMuFi (Grant No. FP6-03321) for financial support.

*Corresponding author; b.j.kooi@rug.nl

[1] N. Hur, S. Park, P. A. Sharma, J. S. Ahn, S. Guha, and S.-W. Cheong, Nature (London) **429**, 392 (2004).
[2] M. Fiebig, J. Phys. D: Appl. Phys. **38**, R123 (2005).
[3] T. Kimura, T. Goto, H. Shintani, K. Ishizaka, T. Arima, and Y. Tokura, Nature (London) **426**, 55 (2003).
[4] J. A. Alonso, M. J. Martinez-Lope, and M. T. Casais, Inorg. Chem. **39**, 917 (2000).
[5] T. Kimura, G. Lawes, T. Goto, Y. Tokura, and A. P. Ramirez, Phys. Rev. B **71**, 224425 (2005).
[6] T. Goto, T. Kimura, G. Lawes, A. P. Ramirez, and Y. Tokura, Phys. Rev. Lett. **92**, 257201 (2004).
[7] D. Rubi, C. de Graaf, C. J. M. Daumont, D. Mannix, R. Broer, and B. Noheda, Phys. Rev. B **79**, 014416 (2009).
[8] X. Marti, V. Skumryev, A. Cattoni, R. Bertacco, V. Laukhin, C. Ferrater, M. V. Garcia-Cuenca, M. Varela, F. Sanchez, and J. Fontcuberta, J. Magn. Magn. Mater. **321**, 1719 (2009).
[9] B. J. Kirby, D. Kan, A. Luykx, M. Murakami, D. Kundaliya, and I. Takeuchi, J. Appl. Phys. **105**, 07D917 (2009).
[10] C. J. M. Daumont, D. Mannix, Sriram Venkatesan, G. Catalan, D. Rubi, B. J. Kooi, J. Th. M. De Hosson, and B. Noheda, J. Phys.: Condens. Matter **21**, 182001 (2009).
[11] C. Daumont, Ph.D. thesis, University of Groningen, 2009.
[12] S. Venkatesan, A. Vlooswijk, B. J. Kooi, A. Morelli, G. Palasantzas, J. T. M. De Hosson, and B. Noheda, Phys. Rev. B **78**, 104112 (2008).
[13] J. Seidel, L. W. Martin, Q. He, Q. Zhan, Y.-H. Chu, A. Rother, M. E. Hawkridge, P. Maksymovych, P. Yu, M. Gajek, N. Balke, S. V. Kalinin, S. Gemming, F. Wang, G. Catalan, J. F. Scott, N. A. Spaldin, J. Orenstein, and R. Ramesh, Nature Mater. **8**, 229 (2009); H. Béa and P. Paruch, *ibid.* **8**, 168 (2009).
[14] The value of δ is obtained by using the formula $\delta = 3.905 \tan(\theta)/2$, where 3.905 is the STO lattice parameter, θ is $(90° - \gamma)$ with γ the pseudocubic angle, i.e., orthorhombic distortion from 90°. The lattice parameter of the film a and b is calculated using the formula $a = \sqrt{(3.905)^2 + (3.905 - 2\delta)^2}$ and $b = \sqrt{(3.905)^2 + (3.905 + 2\delta)^2}$.
[15] C. J. M. Daumont, Sriram Venkatesan, B. J. Kooi, J. Th. M. De Hosson, and B. Noheda (unpublished).